nature portfolio

https://doi.org/10.1038/s41566-022-01011-0

Supplementary information

Nanokelvin-resolution thermometry with a photonic microscale sensor at room temperature

In the format provided by the authors and unedited

Supplementary Information

Nanokelvin-Resolution Thermometry with a Photonic Microscale Sensor at Room Temperature

Amin Reihani[1], Edgar Meyhofer[1,a)], Pramod Reddy[1,2,b)]

[1] *Department of Mechanical Engineering, University of Michigan, Ann Arbor, 48109*

[2] *Department of Materials Science, University of Michigan, Ann Arbor, 48109*

S1. Experimental setup

All experiments were conducted in a vacuum chamber (pressure <5 mTorr) that was in turn located in an ultra-low vibration chamber which was temperature controlled to <100 mK drift over a day. All instruments, including all lock-in amplifiers, were placed in this chamber to minimize thermal drift. The laser employed in the experiments was a QPhotonics QFBGLD-895-2 FBG laser with a maximum power output of 2 mW at 895 nm. This laser is wavelength-stabilized using a fiber Bragg grating. The laser driver was an Arroyo 6301, which allowed precise control of the laser die temperature. The laser and connector were enclosed by an aluminum thermal shield achieving <1 mK temperature stability. The output of the laser was coupled into a single-mode fiber and the fiber's output was collimated into free space using a Thorlabs PAF-X-11-PC-B collimator, passed through a linear polarizer (Thorlabs LPVIS050) to ensure the correct polarization required for the modulator, and fed into an electro-optic amplitude modulator (Thorlabs NEL03) for amplitude stabilization, which enabled achieving a relative intensity noise (RIN) of - 120 dB/Hz at 1 Hz. The output of the modulator was passed through a half-wave plate (Thorlabs WPH10M-915), to rotate

[a)] Electronic mail: meyhofer@umich.edu
[b)] Electronic mail: pramodr@umcih.edu

the polarization as needed, and coupled back to a polarization maintaining single-mode fiber, which was then fed into the vacuum chamber using a fiber vacuum feedthrough (OZ Optics, NEW VAC-01-V-SMJ-3A3A-780-5/125-1-1,0.4). Inside the vacuum chamber, the fiber was connected to a collimator (Schäfter and Kirchhoff 60FC-4-A2.7-02) which couples the light into free space to measure of the resonator reflectance as shown in Fig. 1e. The bow-tie shaped copper chip holder was mounted on a rotational stage (Thorlabs MSRP01/M) allowing adjustment of the incidence angle. The reflected beam was passed through a 200 μm diameter precision pinhole (Thorlabs P200D) to remove reflected rays from the beams with divergence angle >0.5 mrad. This resulted in an improved sensitivity of the thermometer. Finally, identical Si photodiodes (Thorlabs FD11A) were used for the measurement of the reflected and reference beams.

S2. Beam profile and optical alignment

The laser beam alignment was done under atmospheric conditions using a beam profiler (Newport LBP2-HR-VIS2). First, the collimator inside the vacuum chamber (Schäfter and Kirchhoff 60FC-4-A2.7-02) was separately focused to position the beam waist on the surface of the suspended thermometer. Fig. S1a shows the beam profile measured ~40 mm from the collimator (which is the distance of the collimator outlet to the GaAs thermometer) showing a beam diameter of 125 μm. Next, the location of the beam on the thermometer was adjusted to avoid the patterned Pt layer. This alignment was confirmed by ensuring that the reflected beam was a circular Gaussian beam (see Fig. S1b). A similar procedure was employed for aligning the common mode rejection beam when necessary for the lowest power measurements. Finally, the beam profiler was placed behind the device to detect any transmitted light. As can be seen in Fig. S1c, a very small transmitted flux was detected confirming that the beam is well blocked by the Au reflector on the thermometer.

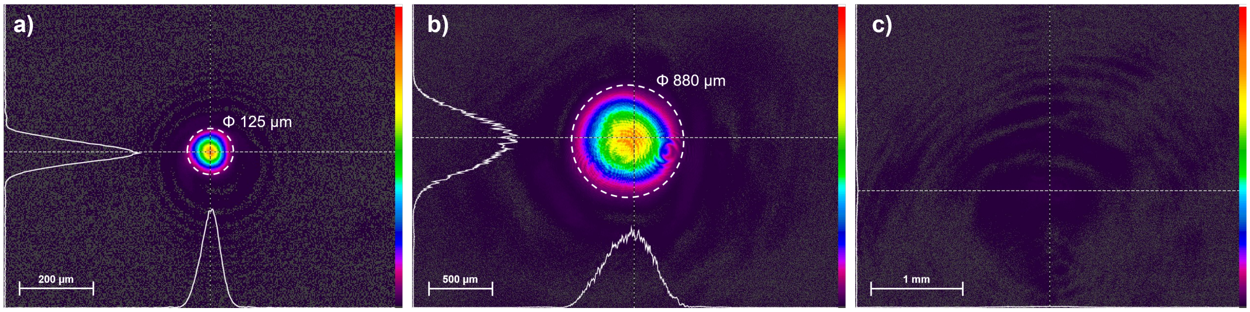

Figure. S1 *Beam intensity profiles. (a) Intensity profile of the beam focused on the suspended thermometer, (b) reflected beam from the suspended thermometer and (c) intensity distribution of the light transmitted through the suspended thermometer.*

S3. Temperature ramp and hysteresis

In order to quantify the repeatability of our band-edge thermometer (BET), the temperature was ramped up and down many times over an extended duration. As an example, Fig. S2a shows an applied temperature ramp up and down (± 0.35 C) around the absorption peak at 32.8 °C at a rate of 2.5 mK/s. The measured DC and AC reflectances are plotted as a function of the resonator temperature (measured by the integrated platinum resistance thermometer (PRT) on the resonator) in Fig. S2b. As can be seen, no significant hysteresis is observed in the reflectance signals, indicating repeatability of the temperature sensing scheme.

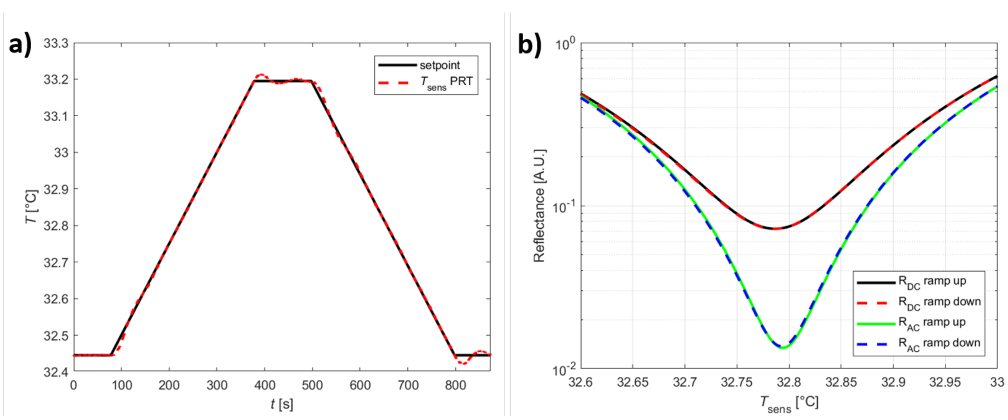

Figure. S2 *(a) The temperature profile of the resonator (T_{sens}) as measured by the integrated platinum resistance thermometer during a ramp up and down protocol. The temperature change corresponds to a rate of 2.5 mK/s. (b) Measured resonator reflectance during a temperature ramp up and down experiment from around the absorption peak of 32.8 °C.*

S4. Quantification of the effect of optical nonlinearities and temperature changes on the sensed temperature in band-edge thermometry

To quantify the effect of laser amplitude fluctuations on the performance of the BET, two separate effects are considered, (a) optical nonlinearity effects of GaAs which result in a reflectance that is dependent on the intensity of the incident beam and (b) temperature fluctuations of the BET due to absorption of the fluctuating incident flux (photothermal absorption), which are discussed below. In general, the laser beam incident on the BET has a time-dependent flux $\phi(t) = \bar{\phi} + \phi_n(t)$, where $\bar{\phi}$ is a steady mean value and $\phi_n(t)$ is the flux noise. Optical non-linearities in GaAs cause variations in the refractive index and absorption coefficient as the incident flux changes[1]. These variation in turn result in a change in the measured reflectance. In addition, the noise in the incident flux perturbs the temperature such that the temperature of the suspended region of the BET is given by $T(t) = \bar{T}(t) + T_n(t)$, where $\bar{T}(t)$ is the temperature of the thermometer at mean flux of $\bar{\phi}$ and $T_n(t)$ is the temperature perturbation caused by the flux noise. Considering these two effects, the reflectance can be represented as:

$$R(\phi, T) = R(\bar{\phi} + \phi_n, \bar{T} + T_n) \approx R(\bar{\phi}, \bar{T}) + \frac{\partial R}{\partial \phi}\phi_n + \frac{\partial R}{\partial T}T_n \qquad (1)$$

In order to experimentally determine the effect of nonlinear absorption and dispersion on reflectance (defined by $\partial R/\partial \phi$ in Eq. 1) we first chose experimental conditions to minimize the thermal effect on reflectance. To this end, the temperature of the chip holder was maintained at a constant value of T_{res} = 32.79 °C, i.e. a temperature that corresponds to a DC thermoreflectance coefficient of zero (i.e. $\frac{1}{R}\frac{\partial R}{\partial T} = 0$). Then, the incident beam intensity was square wave-modulated at 0.5 Hz between the two levels of 10.6 and 31.9 μW using an electro-optic modulator and the incident beam was focused to a spot size with diameter of 125 μm. The measured beam intensity from the reference photodiode, and the resultant reflectance coefficient are shown in Fig. S3. As can be seen, upon a step increase in intensity, the reflectance also increases by a small amount. The average normalized nonlinearity coefficient was estimated from the results of Fig. S3 to be $1/R\ \partial R/\partial\phi \approx 1/\mathrm{R}\ \Delta R/\Delta I = 1.8\times10^{-3}$ (1/μW). This estimated value was later used to calculate the impact of laser amplitude fluctuations on the performance of the BET (see Fig. 4a of the manuscript). Finally, $T_n(t)$ is related to $\phi_n(t)$ via the known thermal response of the device shown in Fig. 3b. Briefly, based on this analysis and further discussion in Section S6, the photothermal absorption and optical non-linearity effects can be a limiting factor to the resolution of the BET if the laser source intensity fluctuations are not well compensated.

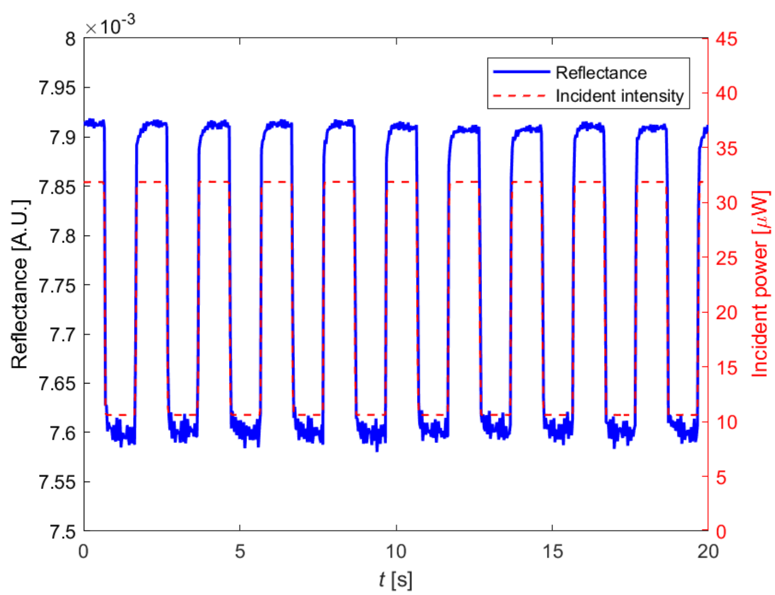

Figure. S3 *Measurement of the effect of optical nonlinearity on reflectance at the resonator absorption peak, i.e. the point of no temperature sensitivity and large absorption. The incident beam was focused to a spot with a diameter of 125 μm. As the incident intensity is increased the reflectance also increases due to nonlinearities in the optical properties as described in the text.*

S5. Sensing of modulated temperatures

In order to quantify the temperature sensing resolution of our BET we heated the suspended region by inputting known amounts of heat, via Joule heating, while measuring the temperature rise via our BET and the integrated PRT. To input known amounts of heat, we applied a square wave-modulated current with an offset ($I = I_{AC}$ (f_{mod}) + I_O) to the integrated Pt ring heater (resistance R_h = 1 kΩ, see Fig. 1a of the manuscript). Here, I_{AC} is the amplitude of the square wave and f_{mod} (1.0 Hz or 2.0 Hz) is the frequency of the square wave and chosen to be comparable to the thermal cut off frequency, while I_O is a nominally constant offset current superimposed on the square current. The applied current can be represented as a Fourier series (sgn represents the sign function) by:

$$I(t) = I_0(t) + I_{AC} sgn(sin(2\pi f_{mod} t)) = I_0(t) + I_{AC}\left(\frac{4}{\pi}\sum_{n=1,3,5,\dots}^{\infty}\frac{1}{\mathrm{n}}\sin\left(2\pi n f_{\mathrm{mod}} t\right)\right) \quad (2)$$

This applied current results in Joule heating described by:

$$p(t) = R_{\mathrm{h}}\left[I_{\mathrm{O}}^2(t) + I_{\mathrm{AC}}^2\right] + 2R_{\mathrm{h}}\, I_{\mathrm{DC}}\, I_{\mathrm{AC}}\left(\frac{4}{\pi}\sum_{n=1,3,5,\dots}^{\infty}\frac{1}{\mathrm{n}}\sin\left(2\pi n f_{\mathrm{mod}} t\right)\right) = p_{\mathrm{O}} + p_{\mathrm{AC}}\,\mathrm{sgn}\left(\sin\left(2\pi f_{\mathrm{mod}} t\right)\right) \quad (3)$$

The first term is Eq. (2) is weakly dependent on time and is labeled $p_{O,}$ which is used via a feedback loop (explained in section S5.1) to ensure that the DC temperature of the suspended region is stabilized close to 32.83 °C that corresponds to the largest sensitivity of the BET (as identified in Fig. 2c of the manuscript). The second term, p_{AC} sgn(sin(2π f_{mod} t)), represents a square wave of deposited power with frequency f_{mod} with peak amplitude $p_{AC} = 2R_h I_{DC} I_{AC}$ that generates small modulations in the temperature (at f_{mod}).

Next, we modulated the intensity of the probe laser beam at f_s = 200 Hz and measured the AC reflectance (R_{AC}) at f_s using a lock-in amplifier in a bandwidth of either 20 or 50 Hz. The output of the lock-in-amplifier was related to the resonator temperature ($\Delta T_{sens}(t)$) via $\Delta T_{sens}(t) = \Delta R_{AC}(t)/(R_{AC}\, k_{AC})$ where k_{AC} is the AC thermoreflectance coefficient. Further, the PRT was also employed to concurrently measure the resonator temperature using a Wheatstone bridge by supplying an AC voltage at 400 Hz with a peak-to-peak amplitude of 1 V, measuring the output of the Wheatstone bridge using a lock-in amplifier (20 Hz bandwidth) and converting the resistance of PRT to temperature as a function of time. Next, we employed a lock-in amplifier to measure (in a bandwidth of 0.1 Hz) the temperature variations corresponding to the frequency f_{mod} (i.e. the frequency at which the Joule heating was modulated).

To further illustrate the performance of our thermometer, we show in Fig. S4 the time-averaged T_{sens} obtained by first locking in to the AC probe beam, which was modulated at f_{s} = 200 Hz, to determine the R_{AC} and then calculating $\Delta T_{\mathrm{sens}}(t) = \Delta R_{\mathrm{AC}}(t)/(R_{\mathrm{AC}}\ k_{\mathrm{AC}})$. In Fig. S4 the sampling frequency of T_{sens} is 20 Hz, obtained from both the band-edge and PRT sensors, when the temperature is modulated at f_{mod} = 2 Hz. To obtain this plot, 100 independent data sets were averaged. As can be seen, the BET clearly shows peak-to-peak temperature modulation of ~7 μK, whereas the PRT signal is very noisy.

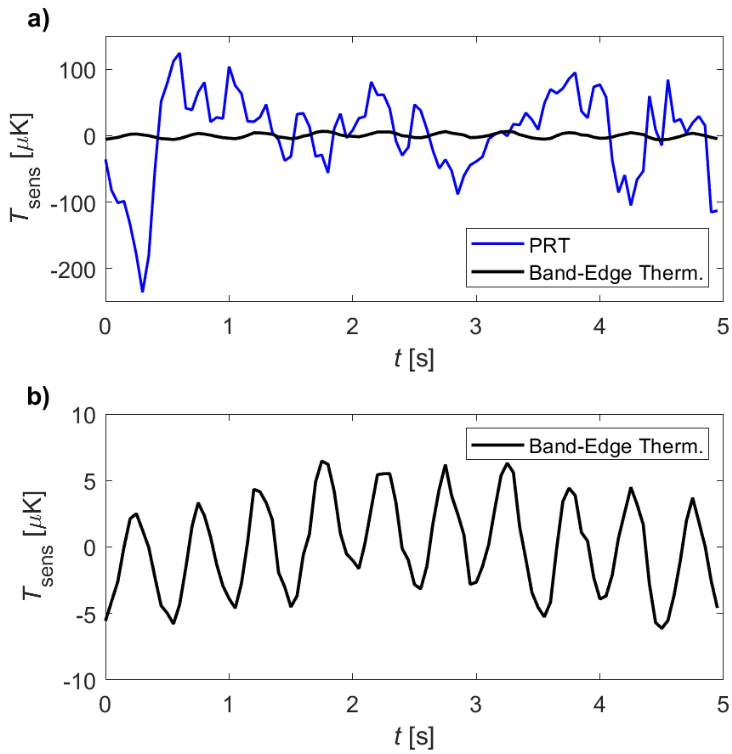

Figure S4. **(a)** *Time-averaged temperature of the suspended region (T_{sens}) as obtained from band-edge thermometry and PRT when the temperature is modulated at f_{mod} = 2 Hz.* **(b)** *Zoomed plot of time-averaged temperature obtained by band-edge thermometer. The sampling frequency of the time series is 20 Hz, and 100 curves were averaged to obtain the plotted curve.*

S5.1. Controllers for attenuating temperature drifts for modulated temperature sensing

The control scheme employed in our measurements is shown in Fig. S5 (a). Here, T_{sens} is the temperature measured using the optical scheme. The two control loops are used to suppress slow and fast components of temperature fluctuations by controlling the temperature of the copper chip holder (Fig. 1c) and the DC temperature of the suspended region, respectively. First, a slow control loop is used to suppress the slow drift (<0.01 Hz) component of T_{sens} by adjusting the power (p_{res}) being input into the copper chip holder shown in Fig.1c. Second, a separate controller is used to suppress the intermediate frequency fluctuations of T_{sens} below the thermal modulation frequency (0.01 Hz to 0.5 f_{mod}) by adjusting the power dissipated (p_{sus}) in the Pt ring heater integrated into the suspended region of the device. The upper bound on the frequency range of this controller ($0.5\,f_{\mathrm{mod}}$) is selected to avoid damping of the modulated temperature via feedback.

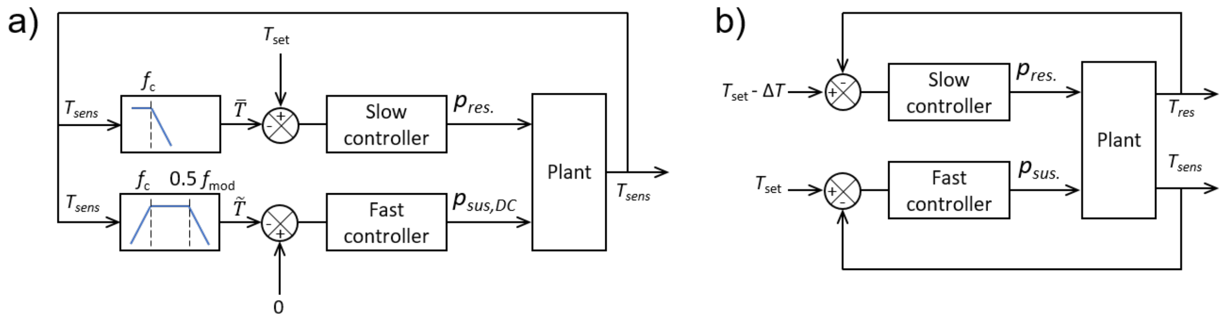

***Figure S5**. Feedback control schemes for temperature stabilization of the suspended thermometer. (a) Characterization of thermometer resolution for modulated temperature sensing at f_{mod}. (b) Unmodulated temperature sensing and stabilization.*

S6. Estimating the theoretical noise floor of band-edge thermometer

In order to understand the ultimate limit to the thermometry noise floor of our current design of the BET, we analyze the relevant noise sources. Specifically, we quantify the contributions of photocurrent shot noise $i_{\mathrm{sn}} = (2qI\Delta f)^{1/2}$, where I is the photodiode current[2], the Johnson noise associated with the feedback resistor (R_{f}) of the transimpedance amplifier[2] $i_{\mathrm{Jn}} = (4k_{\mathrm{B}}T\Delta f/R_{\mathrm{f}})^{1/2}$, and the probe beam intensity noise. In estimating the temperature noise associated with probe beam intensity fluctuations, we include both the contributions from photothermal absorption effect (i.e. the variation in resonator temperature due to fluctuations in deposited laser power) and optical nonlinearity effects (i.e. change in the reflectivity due to variation in beam intensity, see section S4). The intensity noise of the probe beam was measured using the reference photodiode and employed to estimate the photothermal absorption and nonlinearity noises mentioned above. As shown in Fig. S6 (which is a more detailed version of Fig. 4a of manuscript), the thermometry noise floor of the thermometer is limited by photothermal absorption at low frequencies ($f < 0.02$ Hz), and by photocurrent shot noise at higher frequencies. The estimated noise limit, i.e. the sum of the all the aforementioned noise sources, is plotted in red in Fig. 4a of the manuscript, which shows a noise floor of 46 nK/√Hz at $f > 0.2$ Hz. As a point of comparison, we also show the fundamental thermodynamic fluctuation in temperature (dashed green curve in Fig. 4a of manuscript) due to shuttling of phonons from the thermal reservoir to the suspended region, which has a root mean square (RMS) value of $(4k_B T^2/G_{th})^{1/2}$ and a frequency-dependent temperature fluctuation amplitude of $[4k_B T^2/(G_{th}+2G_{th}\pi f\tau_{th})]^{1/2}$ [3].

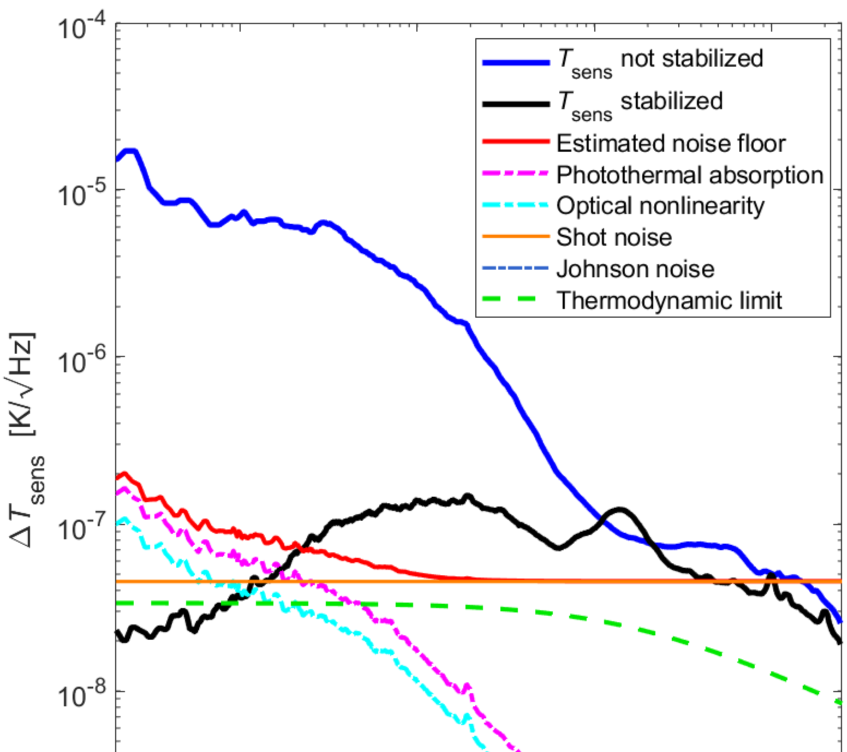

Figure. S6 *Power spectral density of the temperature of the suspended region (T_{sens}) with (black line) and without (blue) feedback stabilization along with the estimated noise floor, which is the sum of shot noise, Johnson noise, photothermal absorption, and optical nonlinearity effects. Further, the estimated noise from thermodynamic fluctuations is also shown (green line). As can be seen, the thermometry noise floor is limited by photothermal absorption (due to probe beam intensity fluctuations) at low frequencies and shot noise at high frequencies.*

S6.1. Temperature stabilization for determination of thermometry noise floor

The temperature stabilization scheme employed by us is shown in Fig. S5 (b) and works as follows. First, the temperature of the copper bow-tie chip holder (T_{res}) is stabilized using a PID controller with a bandwidth of 50 Hz at a setpoint ΔT = 2 mK lower than the desired setpoint (T_{set}) of the suspended reflector (T_{sens}) to provide sufficient dynamic range for T_{sens} heater during long experiments. Second, the temperature of the suspended thermometer (T_{sens}) is measured using the DC reflectance signal of the BET and fed to a separate controller at a bandwidth of 50 Hz to stabilize the T_{sens}. This scheme was used for temperature stabilization in Fig. 4a of the manuscript.

S7. Optical modeling of the thermometer

We employed a numerically stable scattering matrix approach[4] that enables us to exactly solve Maxwell's equations to obtain the reflectivity from multilayer structures. We modeled the reflectance of a structure consisting of 130 μm undoped GaAs coated with 300 nm Au on the back side, corresponding to the geometry of the thermometer used in this study, when a p-polarized beam at 895 nm is incident at 30° on the structure. The scattering matrix model requires input of the dielectric properties of each layer as a function of temperature. For the Au reflector layer, the dielectric constant (ε_r = -32.294 + 1.9516i) was obtained from Ref. [5] and we assumed no temperature dependence. The temperature-dependent dielectric properties of GaAs at the Urbach edge (895 nm) were obtained as explained below. First, we obtain the temperature-dependent band gap (E_g) using Eq. 4 with empirical parameters; E_B = 1.571 eV, a_B = 0.057 eV, and Θ = 240 K [6]. This E_g was later used in Eq. 5, which is valid in the Urbach region [7], to estimate the absorption coefficient (α). In Eq. 5, $h\nu$ is the incident photon energy, E_0 is the width of the absorption edge, and α_g is the absorption coefficient exactly at bandgap, which is 8000 cm^{-1} for GaAs[7] and is fixed in our model. The refractive index was modeled as a parabolic polynomial as a function of the difference of photon energy and band gap as shown in Eq. 6, where n_0 is the extrapolated refractive index at bandgap based on the fit and is fixed at 3.665, which is in good agreement with Ref. [8]. Please note that the functional form of the refractive index considered here is only valid in a small range of bandgap energy variation (~10 meV) in the 20-42 °C temperature range that was used in this study, for larger energy variations other functional forms such as the Sellmeier equation should be used [9].

$$E_g(T) = E_B - a_B\left[1 + \frac{2}{e^{\Theta/T} - 1}\right] \tag{4}$$

$$\alpha(h\upsilon) = \alpha_g \exp\left(\frac{h\upsilon - E_g}{E_0}\right) \tag{5}$$

$$n(h\upsilon) = n_0 + n_1\left(h\upsilon - E_g\right) + n_2\left(h\upsilon - E_g\right)^2 \tag{6}$$

The free parameters of this model are; E_0, n_1, n_2, and ΔT_{offset}, where ΔT_{offset} is the temperature offset of the sensor compared to absolute value of temperature used in the model. These parameters were obtained by fitting the DC reflectance to the experimental results (of Fig 2a) using nonlinear constraint optimization (FMINCON)[10] in MATLAB. The parameters of the model were constrained to vary within a reasonable range of previous measurements in Ref. [7] and [11], and the temperature offset was allowed to vary in the range of -2 to 2 °C. Finally, since the DC reflectance was modeled, a constant background reflectance equal to the background obtained from experimental results was added to the modelled reflectance; $R_{model} = R_{scattering\ matrix} + R_{BG}$. The fitted parameters of the model are, E_0 = 6.51 meV, n_1 = 3.182 eV^{-1}, n_2 = 16.8 eV^{-2}, and ΔT_{offset} = 0.1 K, which are in the range of previous measurements[7,8]. For instance, the value of E_0 from Ref. [7] is ~7.5 meV, and a parabolic fit (similar to Eq. 6) to the refractive index data in Ref. [8] leads n_0 = 3.664, n_1 = 2.603 eV^{-1}, and n_2 = 22.117 eV^{-2}. The agreement of the fitted model parameters with the previously reported values as well as the good agreement of modelled resonator reflectance and experimental measurements indicate the validity of the physical model employed here.

S8. Estimation of the footprint area for different sensors

In order to estimate the sensor footprint area of all the devices listed in Fig. 4b, we attempted to consistently identify the active portion of the sensor which has to thermalize (i.e. reach local thermal equilibrium) with the system of interest whose temperature needs to be measured. For the BET, the region of the resonator where the temperature measurement is performed represents the area which needs to thermalize with the system of interest and thus limits the smallest lateral dimensions of the sensor. In the current experimental setup, the beam spot diameter is ~125 μm as directly measured (explained in Section S2) and was used for estimating the sensor footprint area.

To estimate the sensor footprint area of the resonant cavity mode thermometer[12], the dimensions of main cavity (length 100 mm and diameter of ~25 mm), which has to thermalize with the environment, were used ignoring the reference cavity footprint since it can be placed outside the desired sensing region. Next, for the whispering-gallery mode (WGM) resonators[13,14], the resonator needs to thermalize with the environment for temperature sensing. Therefore, the resonator diameter, which ultimately limits the lateral dimensions of the sensor, was used to estimate the footprint. We note, that in making this estimate, we ignored the required coupling components such as prism, fiber, or waveguide couplers, which need to be positioned adjacent to the WGM resonator[15], as they do not need to thermalize with the system of interest.

Next, when analyzing a fiber loop mirror[16] based temperature sensor, the region that needs to thermalize is the photonic crystal fiber, which had a length of 61 mm and a diameter of ~120 μm. Similarly, for a liquid-in-glass thermometer[17], the length (23 mm) and the inner diameter (0.75 mm) of the capillary tube, which needs to thermalize with the environment for temperature sensing, were used to calculate the footprint area. For the bimaterial cantilever thermometer[18], the suspended cantilever needs to thermalize for temperature sensing which has an area of 200×50 μm^2, whereas for the PM fiber resonator thermometer[19], the entire fiber ring needs to thermally equilibrate with the environment to sense the temperature, which has a length of 2000 mm and a fiber cladding diameter of 125 μm, which were used for estimating the footprint area.

We analyzed thermistors[20,21] by considering their footprint when placed on a surface (i.e. sensor length × width) was used, ignoring the electrical connection leads, while for platinum resistance thermometers[22], a footprint area of ~50×50 μm^2 was obtained by estimating the area needed to fit a serpentine pattern with a resistance of ~10 kOhm. Finally, for quartz crystal thermometers[23], we estimated the sensor dimensions (6.7×2.6 mm^2) from the Statek Corp. Ultra Miniature surface mount crystal.

References

1 Lee, Y.-H. *et al.* Room-temperature optical nonlinearities in GaAs. *Physical Review Letters* **57**, 2446 (1986).

2 Masalov, A., Kuzhamuratov, A. & Lvovsky, A. Noise spectra in balanced optical detectors based on transimpedance amplifiers. *Review of Scientific Instruments* **88**, 113109 (2017).

3 McCammon, D. *et al.* Thermal calorimeters for high resolution X-ray spectroscopy. *Nuclear Instruments and Methods in Physics Research Section A: Accelerators, Spectrometers, Detectors and Associated Equipment* **326**, 157-165 (1993).

4 Whittaker, D. & Culshaw, I. Scattering-matrix treatment of patterned multilayer photonic structures. *Physical Review B* **60**, 2610 (1999).

5 Johnson, P. B. & Christy, R.-W. Optical constants of the noble metals. *Physical Review B* **6**, 4370 (1972).

6 Lautenschlager, P., Garriga, M., Logothetidis, S. & Cardona, M. Interband critical points of GaAs and their temperature dependence. *Physical Review B* **35**, 9174 (1987).

7 Johnson, S. & Tiedje, T. Temperature dependence of the Urbach edge in GaAs. *Journal of Applied Physics* **78**, 5609-5613 (1995).

8 Schaefer, S., Gao, S., Webster, P., Kosireddy, R. & Johnson, S. Absorption edge characteristics of GaAs, GaSb, InAs, and InSb. *Journal of Applied Physics* **127**, 165705 (2020).

9 Gehrsitz, S. *et al.* The refractive index of $Al_xGa_{1-x}As$ below the band gap: accurate determination and empirical modeling. *Journal of Applied Physics* **87**, 7825-7837 (2000).

10 Byrd, R. H., Hribar, M. E. & Nocedal, J. An interior point algorithm for large-scale nonlinear programming. *SIAM Journal on Optimization* **9**, 877-900 (1999).

11 Ozaki, S. & Adachi, S. Spectroscopic ellipsometry and thermoreflectance of GaAs. *Journal of Applied Physics* **78**, 3380-3386 (1995).

12 Tan, S., Wang, S., Saraf, S. & Lipa, J. A. Pico-Kelvin thermometry and temperature stabilization using a resonant optical cavity. *Optics Express* **25**, 3578-3593 (2017).

13 Weng, W. *et al.* Nano-Kelvin thermometry and temperature control: beyond the thermal noise limit. *Physical Review Letters* **112**, 160801 (2014).

14 Strekalov, D., Thompson, R., Baumgartel, L., Grudinin, I. & Yu, N. Temperature measurement and stabilization in a birefringent whispering gallery mode resonator. *Optics Express* **19**, 14495-14501 (2011).

15 Cai, L., Pan, J. & Hu, S. Overview of the coupling methods used in whispering gallery mode resonator systems for sensing. *Optics and Lasers in Engineering* **127**, 105968 (2020).

16 Qian, W. *et al.* High-sensitivity temperature sensor based on an alcohol-filled photonic crystal fiber loop mirror. *Optics Letters* **36**, 1548-1550 (2011).

17 David, R. & Hunter, I. W. A liquid-in-glass thermometer read by an interferometer. *Sensors and Actuators A: Physical* **121**, 31-34 (2005).

18 Sadat, S. *et al.* Room temperature picowatt-resolution calorimetry. *Applied Physics Letters* **99**, 043106 (2011).

19 Loh, W., Yegnanarayanan, S., O'Donnell, F. & Juodawlkis, P. W. Ultra-narrow linewidth Brillouin laser with nanokelvin temperature self-referencing. *Optica* **6**, 152-159 (2019).

20 Hur, S., Mittapally, R., Yadlapalli, S., Reddy, P. & Meyhofer, E. Sub-nanowatt resolution direct calorimetry for probing real-time metabolic activity of individual *C. elegans* worms. *Nature Communications* **11**, 1-9 (2020).

21 Festa, C. Thermostat with ±0.5 μK monitoring sensitivity. *Journal of Physics E: Scientific Instruments* **16**, 683 (1983).
22 Sadat, S., Meyhofer, E. & Reddy, P. High resolution resistive thermometry for micro/nanoscale measurements. *Review of Scientific Instruments* **83**, 084902 (2012).
23 Benson, B. B. & Krause Jr, D. Use of the quartz crystal thermometer for absolute temperature measurements. *Review of Scientific Instruments* **45**, 1499-1501 (1974).